ACS OMEGA

http://pubs.acs.org/journal/acsodf

Article

Nonthermal Plasma-Enhanced Chemical Vapor Deposition of Two-Dimensional Molybdenum Disulfide

Chad A. Beaudette,* Jacob T. Held, K. Andre Mkhoyan, and Uwe R. Kortshagen*

Cite This: *ACS Omega* 2020, 5, 21853−21861

Read Online

ACCESS | Metrics & More | Article Recommendations | Supporting Information

ABSTRACT: Molybdenum disulfide (MoS_2) is being studied for a wide range of applications including lithium-ion batteries and hydrogen evolution reaction catalysts. In this paper, we present a single-step nonthermal plasma-enhanced chemical vapor deposition (PECVD) process for the production of two-dimensional MoS_2. This method provides an alternative route to established CVD and plasma synthesis routes. The approach presented here synthesizes films in only a few minutes using elemental sulfur (S_8) and molybdenum pentachloride ($MoCl_5$) as precursors. Deposition utilizes a nonthermal inductively coupled plasma reactor and temperatures around 500 °C. Film growth characteristics and nucleation are studied as a function of precursor concentrations, argon flow rate, plasma power, and deposition time. Few-layer two-dimensional (MoS_2) films were formed at low precursor concentrations. Films with nanoparticle-like features were formed when the precursor concentration was high. Noncontinuous nonstoichiometric films were found at low plasma power, while high plasma power led to continuous films with good stoichiometry. The vacancies and defects in these films may provide active sites for hydrogen evolution.

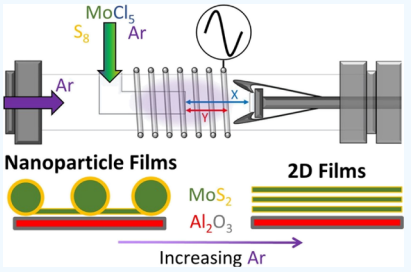

1. INTRODUCTION

MoS_2 has found a wide range of uses in applications including transistors,[1,2] flexible electronics,[3,4] optoelectronics,[5] biological applications,[6,7] lithium-ion batteries,[8] and hydrogen evolution reaction (HER) catalysts.[9,10] However, the optimal morphology of an MoS_2 film is heavily dependent on the application: for HER catalysts, sulfur vacancies, surface defects, and high surface area structures are desired,[10] whereas for transistors, single-crystal defect-free monolayer MoS_2 is required.[11]

Chemical vapor deposition (CVD) has been used to produce large single-crystal grains of MoS_2.[12] However, many authors have reported different grain sizes, layer thicknesses, and crystal shapes with few changes to synthesis conditions.[13−18] Furthermore, the high temperatures required make this process poorly suited for producing films on thermally budgeted substrates and the long reaction times are also undesirable. This has led to the development of alternative synthesis routes for MoS_2, many of which are low-temperature routes.

Low-temperature syntheses of MoS_2 often involve long reaction times, postannealing, the use of hazardous hydrogen disulfide (H_2S), and often produce multilayered films. Atomic layer deposition (ALD) methods can deposit MoS_2 at low temperatures but either requires some form of postannealing to improve the crystallinity of the samples[19−21] or produces rough films at low temperatures.[22] Exfoliation methods are not suitable for the production of large-area films that are required for many industrial applications.[23,24] Low-temperature metal−organic CVD has been the most successful technique for producing ultrathin two-dimensional films at low temperatures with short reaction times on the order of minutes.[25]

Plasma methods, on the other hand, have been effective at low-temperature deposition of MoS_2 but require long reaction times,[26,27] hazardous chemicals (H_2S),[19−22,25−29] and tend to produce multilayer or rough films.[19,21,22,26,27,29] Typically, molybdenum (Mo) is predeposited onto a substrate, which is then exposed to a H_2S plasma to produce multilayer MoS_2 at low temperatures.[27,29] These techniques tend to be the most effective for low-temperature synthesis of few-layer MoS_2. Sputtering techniques have been developed but produce multilayer and randomly oriented films.[26,30] Recently, plasma-enhanced ALD has been applied to grow films at low temperature,[28,31] but it still requires the use of H_2S and often produces multilayered films with randomly oriented vertical structures. Plasma processes have also been applied to the modification of MoS_2 thin films. Such reports include the ability to selectively remove sulfur,[32] create new materials within a monolayer,[33] induce phase transitions,[34] engineer defects,[9] and selectively etch monolayers.[35]

A single-step plasma-enhanced CVD (PECVD) method as a quick and lower-temperature route to both few-layer two-dimensional MoS_2 films would be highly desirable, especially when combined with other plasma modification techniques[9,32−39] in a single chamber. However, such a single-step

Received: June 18, 2020
Accepted: August 6, 2020
Published: August 20, 2020

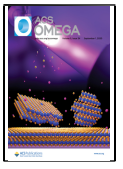

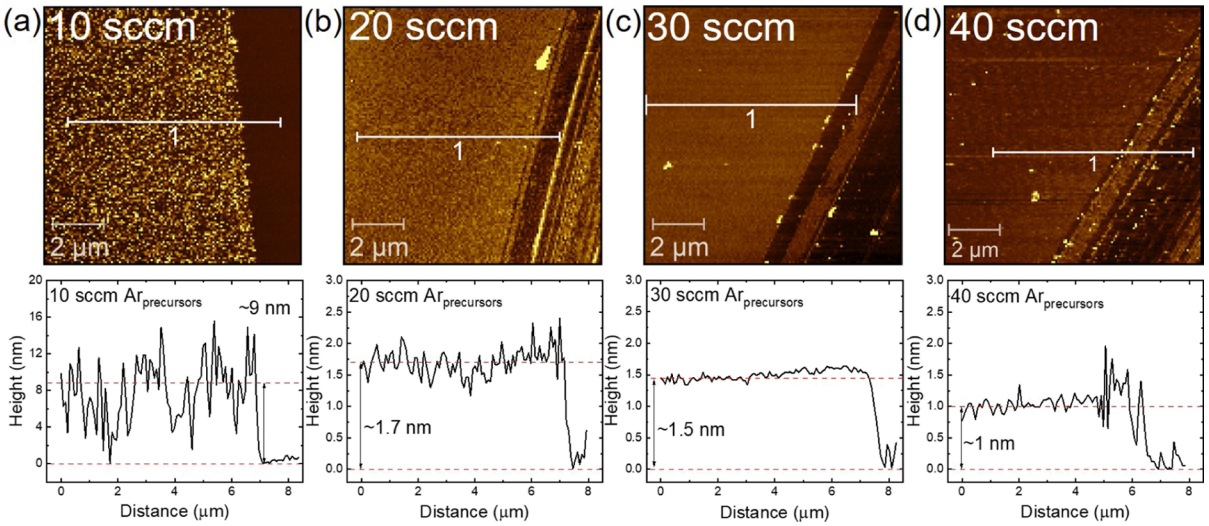

Figure 1. AFM height profiles of MoS_2 films on sapphire (Al_2O_3) as the flow rate of Ar through the precursors ($Ar_{precursors}$) is adjusted. Note the different scale bar on (a) compared to those of (b–d): (a) 10 sccm $Ar_{precursors}$, (b) 20 sccm $Ar_{precursors}$, (c) 30 sccm $Ar_{precursors}$, and (d) 40 sccm $Ar_{precursors}$.

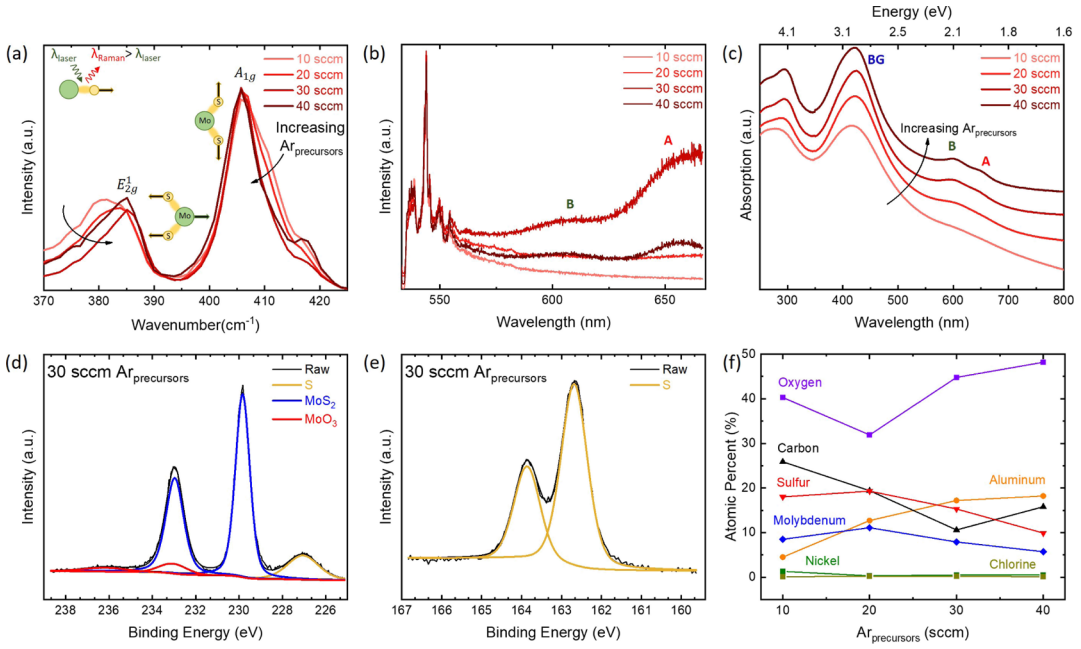

Figure 2. (a) Raman intensity changes based on $Ar_{precursors}$ flow rate. (b) 532 nm Raman laser PL of the films. (c) UV–vis absorption data for films based on $Ar_{precursors}$ flow rate. (d) XPS peaks for Mo 3d orbitals. (e) XPS peaks for sulfur 2p orbitals. (f) XPS survey scans taken at 280 eV pass energy. All data were taken from MoS_2 on sapphire (Al_2O_3).

nonthermal plasma process for two-dimensional MoS_2 films to date has not been reported.

In this paper, we address some of the issues of long process times and hazardous H_2S by demonstrating a fast single-step nonthermal plasma synthesis of MoS_2. The process utilizes two solid precursors, molybdenum pentachloride ($MoCl_5$) and elemental sulfur (S_8), with process times on the order of a few minutes. By tuning precursor concentrations in the gas phase, the process can be controlled to deposit few-layer two-dimensional MoS_2 films or MoS_2 films with nanoparticle-like features. We examine the correlation between film morphologies and process parameters such as the precursor flow rates, plasma power, and process duration. Films are characterized with standard techniques including Raman spectroscopy, UV–visible spectroscopy (UV–vis), X-ray photoelectron spectroscopy (XPS), scanning transition electron microscopy (STEM), and atomic force microscopy (AFM).

2. RESULTS AND DISCUSSION

2.1. Film Properties and Influence of Precursor Flow.

Figures 1–3 demonstrate the ability of our plasma process to deposit MoS_2 both in the form of a two-dimensional material and in the form of films containing nanoparticle-like features. The flow rate of the precursors was found to play a significant role in controlling the morphology of the films.

Figure 1 shows the film morphology determined by AFM for different Ar flow rates through the sulfur sublimator ($Ar_{precursors}$) while holding all other parameters constant. The

https://dx.doi.org/10.1021/acsomega.0c02947
ACS Omega 2020, 5, 21853–21861

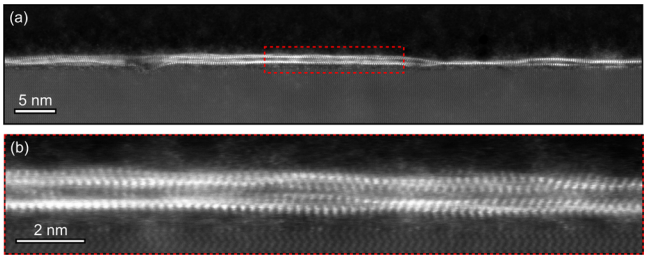

Figure 3. Cross-sectional HAADF-STEM analysis of an MoS_2 film on sapphire (Al_2O_3) produced with 2 min of deposition time, 137 W of power, and 5 sccm $Ar_{precursors}$ flow. (a) Low-magnification image showing the morphology of the film. (b) Magnified image of the highlighted region in (a).

evolution from rough nanoparticle-like films, Figure 1a, to few-layer MoS_2 films, Figure 1c, is shown. These images demonstrate that nucleation of both high surface area and smooth two-dimensional films is possible in a single reactor. This transition, from nanoparticle-like films to smooth two-dimensional films, occurs when the flow rate of $Ar_{precursors}$ through the sulfur bubbler is increased, which decreases the gas-phase concentration of sulfur and molybdenum chloride species relative to the total amount of Ar. The vapor pressure of these precursors is limited by their rate of evaporation, and as the $Ar_{precursors}$ flow rate is increased, these sublimating precursors cannot increase their vapor pressure in the gas phase quickly enough to maintain the previous concentration. The result is a reduction in the vapor pressure of these precursors because of the increased flow rate of $Ar_{precursors}$, which dilutes the precursor vapor in Ar. Temperature differences cannot account for this change because they are negligible over this range as the $Ar_{precursors}$ flow is increased (Figure 7). The impact of the precursor concentration on the film morphology will be discussed further in the text.

To verify the identity and two-dimensional characteristics of the films, XPS, Raman spectroscopy, and UV−vis spectroscopy were used. Figure 2a depicts Raman scattering with a 532 nm laser from the films produced at various $Ar_{precursors}$ flow rates. The films produced at flow rates of 30 and 40 standard cubic centimeter per minute (sccm) exhibit A_{1g} modes at 405.7 cm^{-1}, which correspond to a film of three monolayers,[40] while the frequency difference of 20.63 cm^{-1} between the A_{1g} and E_{2g} modes is also consistent with a two-dimensional MoS_2 thin film.[41] The films produced at 10 and 20 sccm show A_{1g} modes, 405.7 and 406.9 cm^{-1}, that are consistent with a film that consists of three and four monolayers, respectively.[40] The 10 and 20 sccm samples exhibit frequency shifts of 24.3 and 21.8 cm^{-1}, which correspond to quad- and bilayer films, respectively.[41] Peaks located at 378 and 418 cm^{-1} are consistent with those of the underlying sapphire substrate.[42]

A 532 nm Raman laser was used to excite photoluminescence (PL) of the 30 and 40 sccm $Ar_{precursors}$ films (Figure 2b).[40,43] The two PL peaks are located at roughly 670 and 630 nm and correspond to the A and B direct excitonic transitions.[44] The strongest PL is associated with the film that has 1.5 nm thickness (30 sccm) rather than the thinnest 1 nm (40 sccm) film, likely because of the defects in the thinner film whose surface is much rougher than that of the 1.5 nm film, Figure 1c,d.

UV−vis absorption peaks were consistent with a monolayer film, as indicated in Figure 2c. The background (BG) peak is located at roughly 2.9 eV (420 nm), which is consistent with that reported for two-dimensional MoS_2.[44] The A and B excitons indicate direct transitions at the *K* point of the Brillouin zone. The A exciton is located at 1.89 eV and the B exciton is located at 2.08 eV for both samples, consistent with two-dimensional film absorption.[44]

High-angle annular dark-field scanning transmission electron microscopy (HAADF-STEM) was used to examine the

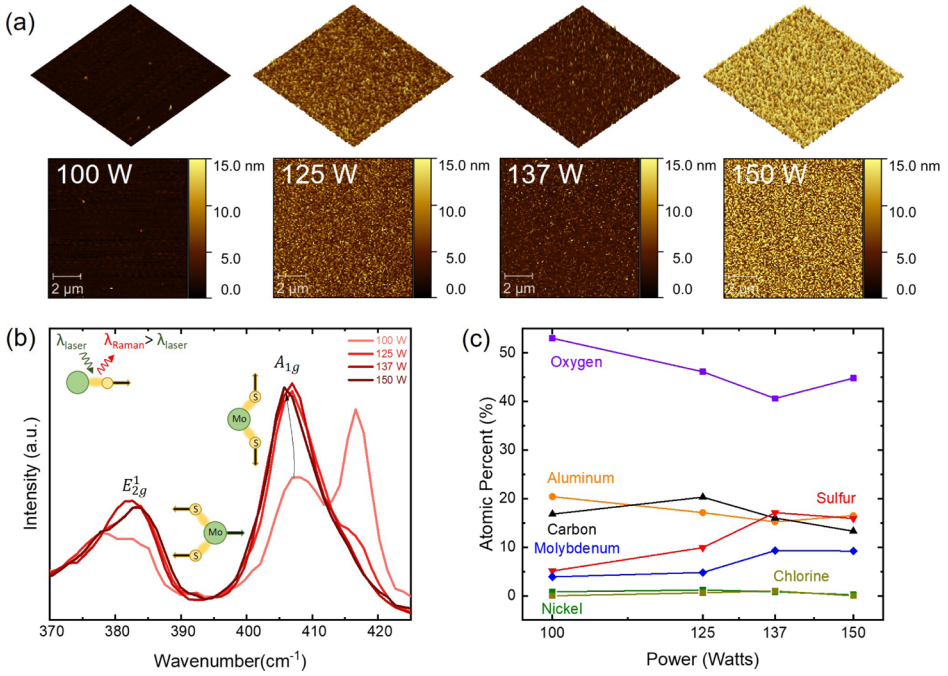

Figure 4. (a) MoS_2 films on sapphire (Al_2O_3) as a function of input power using a high precursor concentration (5 sccm $Ar_{precursors}$). (b) Raman signals of the films as a function of power, which are indicative of three to four layers of MoS_2. (c) Chemical composition derived from XPS survey scans showing the atomic percentages of various elements as a function of input power.

https://dx.doi.org/10.1021/acsomega.0c02947
ACS Omega 2020, 5, 21853−21861

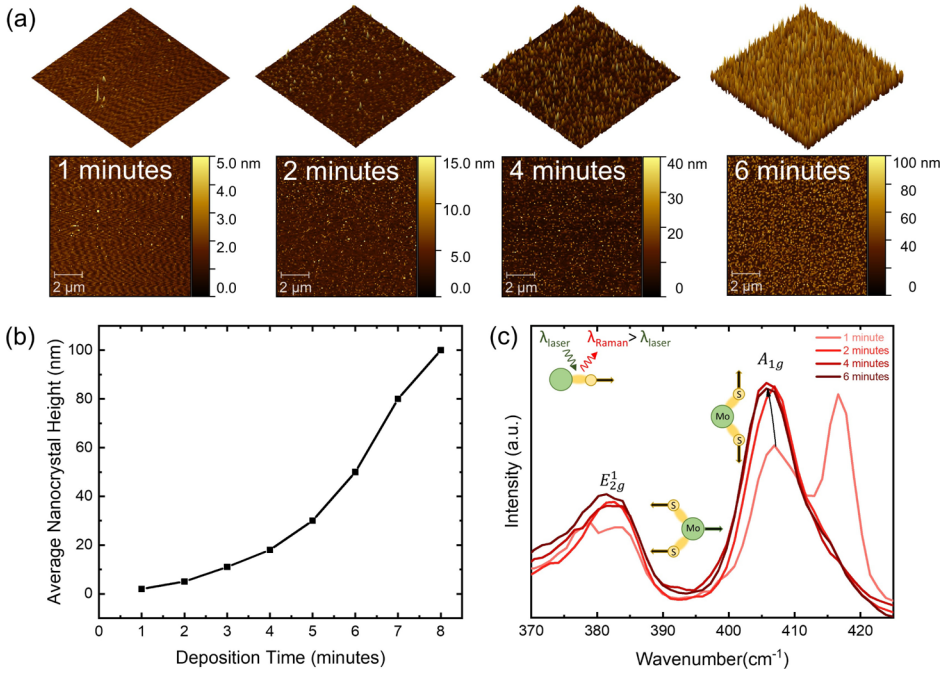

Figure 5. (a) MoS_2 nanoparticle-like films on sapphire (Al_2O_3) produced at 5 sccm $Ar_{precursors}$ flow as a function of plasma deposition time. (b) Average nanocrystal height on the surface of the film as a function of time. (c) Raman intensity signals as a function of time.

structure of an MoS_2 film produced at 5 sccm of $Ar_{precursors}$, 137 W of power, and 2 min of deposition. The HAADF-STEM images in Figure 3 show that the film contains between 1 and 2 monolayers of MoS_2 with lateral grain sizes of approximately 10−30 nm. The films include a high concentration of defects,[45] as shown by the irregular structure in Figure 3b. Furthermore, amorphous nanoparticle-like structures are found in a few locations across the surface of the sample shown in Figures 3b and S1. From these images, it appears that Raman peaks are from the underlying MoS_2 films because of the amorphous nature of the nanoparticle-like features. A damaged portion of the underlying sapphire substrate is also shown in Figure 3a. This phenomenon could be due to chemical or physical etching within the plasma during material synthesis or from the focused ion beam (FIB) used during sample preparation for STEM. Most of the analysis utilized AFM because of the difficulties in sample preparation for STEM.

Figure 2d−f shows the results of the XPS analysis of a film produced at a flow of 30 sccm of $Ar_{precursors}$. These data contain information about the molybdenum (Mo) and sulfur (S) binding energies, which allowed for the determination of the chemical composition of the films. Peak locations at 229.8 and 232.9 eV are consistent with those of MoS_2 bonding.[46] Peak locations for MoO_3 are found at 233.1 eV.[47] Features at 162.7 and 163.8 eV of S binding to Mo further confirm the presence of MoS_2.[46] To confirm the overall film composition and measure any possible contaminants, XPS survey scans at 280 eV were performed (Figure 2f). Contaminants of nickel (Ni) and chlorine (Cl) were on the order of 1% or lower, and carbon (C) content was consistent with films exposed to open air for extended periods of time. Aluminum and oxygen peaks are attributed to the underlying sapphire (Al_2O_3) substrate, unless specified elsewhere. The Ni 201 alloy substrate holder is the source of Ni contamination. We point out that thicker films did contain a few NiS particles and contaminants, although their total percentage of the film was small as indicated by the XPS data.

2.2. Effect of Plasma Power. Plasma power was varied in order to understand its relation to film growth and stoichiometry at 5 sccm $Ar_{precursors}$ flow rate. Film morphology, chemical composition, and density of surface grains change with increasing power, as shown in Figure 4a,c. At 100 W, the substrate surface is poorly covered and contains few nanoparticle-like features (Figure 4a). Although MoS_2 peaks are evident, the largest peak is that from the underlying sapphire substrate at 417 cm^{-1} (Figure 4b). Although, at 125 W, nanoparticle structures are present, the Raman mode at 417 cm^{-1} indicates that the substrate is not completely covered. Increasing the power further causes a reduction in the average surface height and a more consistent coverage of the substrate, as indicated by the disappearance of the sapphire-related peak.

The films produced at low power had an S/Mo ratio of roughly 1:1, as shown in Figure 4c. As the power is increased, the Raman modes for sapphire at 417 cm^{-1} start to disappear until the power reaches 137 W (Figure 4b), and the S/Mo ratio increases to 1.93:1 at 137 W (Figure 4c). These results indicate that a minimum power level is essential for dissociating S. Nonetheless, increasing the power to 150 W reduces the S/Mo ratio slight. Ni and Cl contaminants remained around 1% for all films produced and Cl became undetectable at 150 W (Figure 4c).

Chlorine contamination in all of the produced samples is at or below 1% (Figures 2 and 4c). This is likely due to a combination of Ar bombardment and Cl etching. Cl radicals that attach to an MoS_x molecule at the surface reduce the molecule's adsorption to the surface and make it easier for incoming Ar ions to sputter it into the gas phase while pure MoS_2 is harder to sputter.[37] Substrate holder contaminants are also reduced to a minimum (below 1%) by using a Cl-resistant Ni 201 alloy substrate holder (Figure 4).[48] The samples produced at 5 sccm $Ar_{precursors}$ flow had the highest

https://dx.doi.org/10.1021/acsomega.0c02947
ACS Omega 2020, 5, 21853−21861

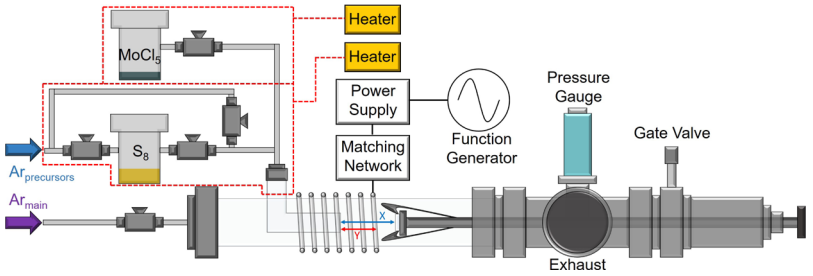

Figure 6. Inductively coupled nonthermal plasma reactor. MoS_2 films are synthesized using Ar, S_8, and $MoCl_5$. $Ar_{precursors}$ represents the Ar flow that carries precursors into the plasma, and Ar_{main} represents the Ar carried in from upstream of the substrate. The substrate is held in place by a Ni 201 alloy clamp near the entrance of the precursor injection point into the plasma, at a distance *X* from the inlet of the precursors. A seven-turn inductive coil, at a distance *Y* from the precursor inlet, is used with a function generator, a power amplifier, and a matching network to produce the plasma. Both precursors and the gas lines are heated up to the entrance to the quartz tube.

contamination from the Ni substrate holder, although it remained on the order of 1% or less.

2.3. Nanoparticle-like Films and Surface Nucleation. From the previous studies, it remains unclear whether or not the roughness observed in Figure 1a is due to the deposition of nanoparticles formed in the gas phase or from the nucleation of particles on the substrate surface. Therefore, a high precursor concentration in the gas phase, associated with a low $Ar_{precursors}$ flow of 5 sccm, was used as such conditions are typically associated with particle growth in the plasma.[49,50]

Figure 5 demonstrates that nanoparticle-like MoS_2 films are observed under the chosen precursor flow rate conditions. These nanoparticle features are better observed under higher-resolution AFM, as shown in Figure S2. After a 1 min deposition, only a few nanoparticle-like features are observed on the substrate, which are rich in Mo (Figures S1 and S3). This suggests that particles are not formed in the gas phase, as nucleation events in the plasma are typically associated with high particle concentrations, on the order of 10^{11} to 10^{12} cm^{-3}.[49,51] Because a significant fraction of the few nanometer-sized particles created during a nucleation event is neutral[51] and thus not trapped by the electric fields in the plasma, a larger concentration of particles should be expected on the substrate after 1 min of deposition.

Depositions for longer times show that the number and size of the nanoparticle-like features on the substrate continue to increase. Figure 5b shows the increase in the average particle size with deposition time. Higher-resolution AFM is shown in Figure S2 for three different times, detailing the profiles of the particle-like features on the surface. The few areas with spikes located on the surface of the nanoparticles are acoustic artifacts and not representative of actual surface morphology.[52] It should be noted that the regions between the particle-like features are devoid of smaller particles, which also suggests that there are no nanoparticles formed through gas-phase nucleation.

Raman scattering indicates that the A_{1g} and E_{2g} modes associated with two-dimensional MoS_2 are present in all films, regardless of the size of the nanoparticle-like features (Figure 5). The A_{1g} and E_{2g} modes are located at 406.9 and 382.6 cm^{-1} for 1 and 2 min deposition films, consistent with four monolayers.[40] The modes shift to 405.7 and 382.6 cm^{-1} for the 4 and 6 min deposition films, consistent with three monolayers.[40] The lack of the sapphire-related peak at deposition times longer than 1 min suggests that the substrate is largely covered with two-dimensional MoS_2 between the particle-like features. The XPS results of these films are provided in Figure S3. All of the above observations suggest a surface nucleation mechanism of the particle-like features, rather than a gas-phase nucleation mechanism.

The transition to smooth films can be interpreted in terms of changes in the surface nuclei and the stoichiometry of the growing films. The films are initially limited by the molybdenum species attaching to, or decomposing on, the surface of the sapphire substrate as the sulfur would re-evaporate at these temperatures. As deposition continues, there is a distinct transition from a surface that contains several Mo-rich nanoparticle-like features at 1 min of deposition (Figures S1 and S3) to a continuous MoS_2 film with larger nanoparticle-like features at 2 min (Figure 5a). These amorphous substoichiometric MoS_x particles have dangling bonds, which pervade the surface. Because of their amorphous nature, the nanoparticle-like features can undergo significant radial and vertical growth while acting as sites for lateral nucleation of crystalline MoS_2 during synthesis (Figure 5a,b).

In order to prevent the formation of larger amorphous substoichiometric MoS_x nanoparticle-like features, we reduced the total concentration of the precursors in the gas phase to reduce the size and growth rate of the initial Mo-rich nanoparticle-like nuclei. This delays the rapid growth of the amorphous structures by allowing more time for these smaller nanoparticle-like nuclei to crystallize and form stoichiometric MoS_2. These crystalline surface MoS_2 nuclei then become the seeds for growth, rather than the larger amorphous features. Because of the lattice match and growth direction, the basal plane of the crystalline MoS_2 is perpendicular to the sapphire substrate which forces growth in the lateral rather than the vertical direction, resulting in ultrathin films, which explains the transition found in Figure 1a–d.

3. CONCLUSIONS

Both smooth few-layer two-dimensional MoS_2 thin films and films with nanoparticle-like features were produced using PECVD with a total process time of 5 min for most films, which is faster than most conventional processes. Furthermore, this process realized Cl-free films without the use of H_2 while utilizing nontoxic elemental sulfur, rather than H_2S, as the sulfur precursor. The morphology of the films was found to vary with the precursor concentration in the gas phase, controlled via the Ar flow rate ($Ar_{precursors}$) through the sulfur sublimator. Few-layer two-dimensional films with minimal particle contamination were grown by utilizing a high $Ar_{precursors}$ flow rate. Films with large nanoparticle-like features could be grown by utilizing a low $Ar_{precursors}$ flow rate. Studies

https://dx.doi.org/10.1021/acsomega.0c02947
ACS Omega 2020, 5, 21853−21861

of different deposition times suggest that the nanoparticle-like features nucleate on the surface rather than in the gas phase.

Few-layer two-dimensional films were characterized with Raman, UV−vis, XPS, and STEM and were found to be consistent with previously reported literature on two-dimensional MoS_2. Plasma power was positively correlated with increasing sulfur incorporation, the rate of film growth, and good MoS_2 stoichiometry. Low plasma powers did not produce continuous films and contained only a few nanoparticle features.

The nonthermal plasma process demonstrated here has offered a fast process for producing MoS_2 films with characteristics that may be advantageous for HER devices as the vacancies and defects in these films may provide active sites for hydrogen evolution. Furthermore, secondary plasma processing could provide options for film modification that may further increase the films' potential for HER catalysts. Although proper precautions, such as the use of a Ni alloy, can mitigate much of the damage and possible contamination caused by the corrosive environment, further design considerations to adjust for continuous operation under such an environment would need to be implemented for industrial applications.

4. METHODS

4.1. Plasma Synthesis Conditions and Reactor Details. MoS_2 thin films are synthesized via a nonthermal PECVD process. The reactor is shown in Figure 6. An inductively coupled plasma (ICP) is excited with a seven-turn copper coil with a length of 3.8 cm that was wrapped around a quartz reactor tube. The quartz tube has the following dimensions: 355 mm length, 25 mm outer diameter, and 21.8 mm inner diameter. The injection port is a 9.6 mm outer diameter quartz tube with a 7 mm inner diameter and is 51 mm in total length inside the reactor. It is located 127 mm from the left end of the reactor and delivers the precursor gas flow to the center of the inductive plasma region. A primary Ar flow (Ar_{main}) is held constant at 30 sccm for all experiments. Heated portions of the reactor are highlighted in red in Figure 6. The sapphire substrate is held by a nickel 201 alloy rod and clamp at a distance of 2.54 cm from the inlet (X in Figure 6) and 0.64 cm (Y in Figure 6) from the 3.8 cm long ICP coil. Reactions are carried out at rough vacuum (220−400 mTorr). The pump used was a D16B Leybold pump with Krytox PFPE oil because of the corrosive nature of Cl released from the Mo precursor.

Two solid precursors are heated to provide sufficient vapor pressure and carried into the reactor via an Ar flow ($Ar_{precursors}$). Molybdenum pentachloride ($MoCl_5$, Sigma-Aldrich 95%) was kept at 80 °C using a BriskHeat heating tape (BWH051040L) and controller (SDC120JC-A) in a metal containment vessel with Swagelock SS-4BG valves. Elemental sulfur (S_8, Alfa-Aesar puratronics 99.9999%) was heated to 120 °C with a BriskHeat heating tape (BWH051080L) and controller (SDC120JC-A) in a vessel with Swagelock SS-4BG valves. The outlets of the S_8 and $MoCl_5$ sublimators meet in a three-way section, which connects to a quartz tube reactor via a quartz to metal weld. All heated elements were connected with SS-VCR or SS Swagelok connections. Ar (99.9993%) ($Ar_{precursors}$) at 5−30 sccm was flown through the sulfur (Alfa Aesar 99.9995% puratronics sulfur) sublimator to carry its vapor into the system. The mass flow of $MoCl_5$ was adjusted through the sublimator temperature; no independent mass flow controller was used. Ar_{main} was maintained at 30 sccm for all experiments.

Although not well known, carbon contamination from elemental sulfur sources can be a very detrimental and a significant contributor to contamination in plasma-produced films.[53] Though a high-purity sulfur precursor was used, this precursor still contains contaminants from hydrocarbons and sulfur oxide compounds[53] at mass fractions on the order of μg/g. Because we are growing atomically thin materials, we have found these contaminants to be significant. Hence, sulfur was purified by first grinding it into a powder and removing all visible black chunks, ostensibly carbon. The sulfur powder was then placed in a glass container and heated to 80 °C for 4 days under air to remove as many remaining hydrocarbons as possible. Prior to running experiments, an initial sacrificial sample was produced under normal running conditions before actually running the rest of the experiments.

To run experiments, sapphire substrates were cleaned with methanol and dried under vacuum. They were then placed on the substrate holder. After the substrate was placed into the reactor, the reactor was allowed to achieve vacuum for 1 min. Then, an ICP was initiated by applying high-frequency power to the induction coil using an ENI A150-1210 power amplifier fed by a Tektronix AFG 3251 arbitrary function generator running between 300 and 700 mVpp, and a Vectronics HFT-1500 matching network.

To produce thin films, power is set to 137 W (nominal power) and the pressure is set to 200 mTorr using 30 sccm Ar_{main} and 30 sccm $Ar_{precursors}$. First, a sapphire substrate is loaded into the vacuum chamber and allowed to rest for 1 min with Ar_{main} flowing at 30 sccm and $Ar_{precursors}$ at 30 sccm. Second, a 137 W ICP in pure Ar is ignited for 1 min. The purpose of this step is to clean the reactor tube and heat up the substrate, as shown in Figure 7, the region with light blue

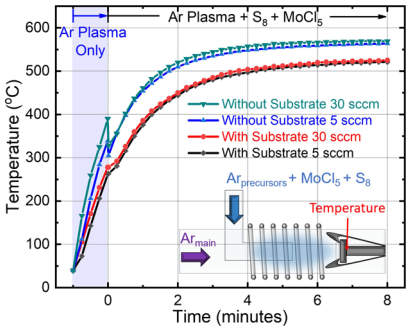

Figure 7. Transient temperature profile of the substrate holder measured with (red circle/black diamond) and without (green down triangle/blue triangle) a substrate in the holder. Temperature measurements were taken at 15 s time intervals using the standard operating procedure for all films at 137 W for two different flow rates of 5 sccm (black diamond/blue triangle) and 30 sccm (red circle/green down triangle) of $Ar_{precursors}$.

background. Third, the plasma is turned off and the precursor valves are opened. Fourth, the ICP is reignited and is sustained for 2 min. Finally, the plasma is turned off and both precursor flows are stopped by closing the valves. The substrate remains in the chamber for 1 min before being removed.

Run conditions for films exhibiting nanoparticle-like features are identical to the thin-film process with the exception of the change in $Ar_{precursors}$ to 5 sccm and deposition time to 2−8 min.

https://dx.doi.org/10.1021/acsomega.0c02947
ACS Omega 2020, 5, 21853−21861

The temperature of the substrate is obviously expected to be an important parameter in the deposition of MoS_2. Unfortunately, because of the heat fluxes associated with the ICP and the thermal mass of the metallic sample holder, it is difficult to achieve a steady substrate temperature or to actively control the temperature. Hence, we adopted the 1 min cleaning/preheating step to raise the substrate temperature before introducing precursors. In Figure 7, the time from −1 to 0 min refers to this clean/preheat stage, followed by actual deposition at times after 0 min that contained an Ar plasma with S_8, $MoCl_5$, and $Ar_{precursors}$ flowing. The figure demonstrates that there is an about 50 °C difference in the temperature measured with and without the substrate in place, likely because of the thermal interface resistance between the substrate and the holder. It should thus be assumed that the substrate temperature is closer to the higher temperatures, that is, the green and blue curves in this figure. The figure also demonstrates that the influence of the flow rate of $Ar_{precursors}$ is small.

4.2. Material Characterization. XPS was conducted on a PHI Versa Probe III XPS and UPS (UV photoelectron spectroscopy) system. High-resolution scans were performed at 55 eV band-pass energy for 10 scans. An Al Kα source was used. A 100 μm spot was used for collection. Data collection was performed under neutralizing ion and electron irradiation (dual-beam charge neutralization). Peaks were adjusted according to the adventitious carbon peak located at 248.8 eV. Subsequent analyses of the peaks were performed using PHI's "Multipak" software. To collect atomic percentages, XPS survey scans were taken at a band-pass energy of 280 eV for five scans. The atomic percentages were then calculated using PHI's "Multipak" software. The analysis procedure for these films can be found in the Supporting Information (Figure S4).

Raman spectroscopy analysis was completed on a Witec Alpha 300R confocal Raman microscope with a 532 nm laser. Spectra were collected with a grating of 1800 grooves/mm with five accumulations of 10 s.

AFM was performed on a Bruker Nanoscope V Multimode 8 with QNM. Images were taken using an n-type silicon tip coated in aluminum (HQ:NSC36/AL BS-15) with a force constant of 0.6 N/m and a resonant frequency of 65 kHz. The peak force tapping mode was used with a frequency of 1 Hz and a force constant between 8 and 20 nN.

Ultraviolet−visible (UV−vis) absorbance measurements were carried out on a Cary 700 UV−vis spectrometer. Corrections were made to the spectrum based on a sapphire background taken prior to data collection.

STEM was performed on an aberration-corrected FEI Titan G2 60−300 STEM operated at 200 kV with a convergence angle of 25 mrad and a beam current of 125 pA. Cross-sectional lamellae of the films were prepared using a Helios NanoLab G4 dual-beam FIB.

■ ASSOCIATED CONTENT

Supporting Information

The Supporting Information is available free of charge at https://pubs.acs.org/doi/10.1021/acsomega.0c02947.

Additional XPS and AFM data (PDF)

■ AUTHOR INFORMATION

Corresponding Authors

Chad A. Beaudette − *Department of Mechanical Engineering, University of Minnesota Twin Cities, Minneapolis, Minnesota, United States;* orcid.org/0000-0002-5708-8133; Email: beaud076@umn.edu

Uwe R. Kortshagen − *Department of Mechanical Engineering, University of Minnesota Twin Cities, Minneapolis, Minnesota, United States;* orcid.org/0000-0001-5944-3656; Email: korts001@umn.edu

Authors

Jacob T. Held − *Department of Chemical Engineering and Materials Science, University of Minnesota Twin Cities, Minneapolis, Minnesota, United States;* orcid.org/0000-0003-3864-4314

K. Andre Mkhoyan − *Department of Chemical Engineering and Materials Science, University of Minnesota Twin Cities, Minneapolis, Minnesota, United States;* orcid.org/0000-0003-3568-5452

Complete contact information is available at: https://pubs.acs.org/10.1021/acsomega.0c02947

Notes

The authors declare no competing financial interest.

■ ACKNOWLEDGMENTS

This work was primarily supported by NSF through the MRSEC program under award DMR-1420013. Part of this work was carried out in the College of Science and Engineering Characterization Facility, University of Minnesota, which has received capital equipment funding from the NSF through the UMN MRSEC program under award DMR-1420013.

■ REFERENCES

(1) Zhu, Y.; Li, Y.; Arefe, G.; Burke, R. A.; Tan, C.; Hao, Y.; Liu, X.; Liu, X.; Yoo, W. J.; Dubey, M.; Lin, Q.; Hone, J. C. Monolayer Molybdenum Disulfide Transistors with Single-Atom-Thick Gates. *Nano Lett.* **2018**, *18*, 3807−3813.

(2) Desai, S. B.; Madhvapathy, S. R.; Sachid, A. B.; Llinas, J. P.; Wang, Q.; Ahn, G. H.; Pitner, G.; Kim, M. J.; Bokor, J.; Hu, C.; Wong, H. S. P.; Javey, A. MoS2 transistors with 1-nanometer gate lengths. *Science* **2016**, *354*, 99−102.

(3) Cheng, R.; Jiang, S.; Chen, Y.; Liu, Y.; Weiss, N.; Cheng, H. C.; Wu, H.; Huang, Y.; Duan, X. Few-layer molybdenum disulfide transistors and circuits for high-speed flexible electronics. *Nat. Commun.* **2014**, *5*, 5143.

(4) Pu, J.; Li, L.-J.; Takenobu, T. Flexible and stretchable thin-film transistors based on molybdenum disulphide. *Phys. Chem. Chem. Phys.* **2014**, *16*, 14996−15006.

(5) Wang, H.; Li, C.; Fang, P.; Zhang, Z.; Zhang, J. Z. Synthesis, properties, and optoelectronic applications of two-dimensional MoS_2 and MoS_2-based heterostructures. *Chem. Soc. Rev.* **2018**, *47*, 6101−6127.

(6) Appel, J. H.; Li, D. O.; Podlevsky, J. D.; Debnath, A.; Green, A. A.; Wang, Q. H.; Chae, J. Low Cytotoxicity and Genotoxicity of Two-Dimensional MoS_2 and WS_2. *ACS Biomater. Sci. Eng.* **2016**, *2*, 361−367.

(7) Yin, W.; Yu, J.; Lv, F.; Yan, L.; Zheng, L. R.; Gu, Z.; Zhao, Y. Functionalized Nano-MoS_2 with Peroxidase Catalytic and Near-Infrared Photothermal Activities for Safe and Synergetic Wound Antibacterial Applications. *ACS Nano* **2016**, *10*, 11000−11011.

(8) Stephenson, T.; Li, Z.; Olsen, B.; Mitlin, D. Lithium ion battery applications of molybdenum disulfide (MoS_2) nanocomposites. *Energy Environ. Sci.* **2014**, *7*, 209−231.

(9) Ye, G.; Gong, Y.; Lin, J.; Li, B.; He, Y.; Pantelides, S. T.; Zhou, W.; Vajtai, R.; Ajayan, P. M. Defects Engineered Monolayer MoS_2 for Improved Hydrogen Evolution Reaction. *Nano Lett.* **2016**, *16*, 1097−1103.
(10) Chen, Y.; Yang, K.; Jiang, B.; Li, J.; Zeng, M.; Fu, L. Emerging two-dimensional nanomaterials for electrochemical hydrogen evolution. *J. Mater. Chem. A* **2017**, *5*, 8187−8208.
(11) Wang, Y.; Kim, J. C.; Wu, R. J.; Martinez, J.; Song, X.; Yang, J.; Zhao, F.; Mkhoyan, A.; Jeong, H. Y.; Chhowalla, M. Van der Waals contacts between three-dimensional metals and two-dimensional semiconductors. *Nature* **2019**, *568*, 70−74.
(12) Gong, Y.; Ye, G.; Lei, S.; Shi, G.; He, Y.; Lin, J.; Zhang, X.; Vajtai, R.; Pantelides, S. T.; Zhou, W.; Li, B.; Ajayan, P. M. Synthesis of Millimeter-Scale Transition Metal Dichalcogenides Single Crystals. *Adv. Funct. Mater.* **2016**, *26*, 2009−2015.
(13) Özden, A.; Ay, F.; Sevik, C.; Perkgöz, N. K. CVD growth of monolayer MoS_2: Role of growth zone configuration and precursors ratio. *Jpn. J. Appl. Phys.* **2017**, *56*, 06GG05.
(14) Cai, Z.; Liu, B.; Zou, X.; Cheng, H.-M. Chemical Vapor Deposition Growth and Applications of Two-Dimensional Materials and Their Heterostructures. *Chem. Rev.* **2018**, *118*, 6091−6133.
(15) Tao, L.; Chen, K.; Chen, Z.; Chen, W.; Gui, X.; Chen, H.; Li, X.; Xu, J.-B. Centimeter-Scale CVD Growth of Highly Crystalline Single-Layer MoS_2 Film with Spatial Homogeneity and the Visualization of Grain Boundaries. *ACS Appl. Mater. Interfaces* **2017**, *9*, 12073−12081.
(16) Lee, Y.-H.; Zhang, X.-Q.; Zhang, W.; Chang, M.-T.; Lin, C.-T.; Chang, K.-D.; Yu, Y.-C.; Wang, J. T.-W.; Chang, C.-S.; Li, L.-J.; Lin, T.-W. Synthesis of large-area MoS_2 atomic layers with chemical vapor deposition. *Adv. Mater.* **2012**, *24*, 2320−2325.
(17) Yu, Y.; Li, C.; Liu, Y.; Su, L.; Zhang, Y.; Cao, L. Controlled scalable synthesis of uniform, high-quality monolayer and few-layer MoS_2 films. *Sci. Rep.* **2013**, *3*, 1866.
(18) Yang, P.; Zou, X.; Zhang, Z.; Hong, M.; Shi, J.; Chen, S.; Shu, J.; Zhao, L.; Jiang, S.; Zhou, X.; Huan, Y.; Xie, C.; Gao, P.; Chen, Q.; Zhang, Q.; Liu, Z.; Zhang, Y. Batch production of 6-inch uniform monolayer molybdenum disulfide catalyzed by sodium in glass. *Nat. Commun.* **2018**, *9*, 979.
(19) Mane, A. U.; Letourneau, S.; Mandia, D. J.; Liu, J.; Libera, J. A.; Lei, Y.; Peng, Q.; Graugnard, E.; Elam, J. W. Atomic layer deposition of molybdenum disulfide films using MoF_6 and H_2S. *J. Vac. Sci. Technol., A* **2018**, *36*, 01A125.
(20) Tan, L. K.; Liu, B.; Teng, J. H.; Guo, S.; Low, H. Y.; Loh, K. P. Atomic layer deposition of a MoS_2 film. *Nanoscale* **2014**, *6*, 10584−10588.
(21) Valdivia, A.; Tweet, D. J.; Conley, J. F. Atomic layer deposition of two dimensional MoS_2 on 150 mm substrates. *J. Vac. Sci. Technol., A* **2016**, *34*, 021515.
(22) Mattinen, M.; Hatanpää, T.; Sarnet, T.; Mizohata, K.; Meinander, K.; King, P. J.; Khriachtchev, L.; Räisänen, J.; Ritala, M.; Leskelä, M. Atomic Layer Deposition of Crystalline MoS_2 Thin Films: New Molybdenum Precursor for Low-Temperature Film Growth. *Adv. Mater. Interfaces* **2017**, *4*, 1700123.
(23) Yin, Z.; Li, H.; Li, H.; Jiang, L.; Shi, Y.; Sun, Y.; Lu, G.; Zhang, Q.; Chen, X.; Zhang, H. Single-layer MoS_2 phototransistors. *ACS Nano* **2012**, *6*, 74−80.
(24) Eda, G.; Yamaguchi, H.; Voiry, D.; Fujita, T.; Chen, M.; Chhowalla, M. Photoluminescence from chemically exfoliated MoS_2. *Nano Lett.* **2011**, *11*, 5111−5116.
(25) Zhao, Y.; Song, J.-g.; Ryu, G. H.; Ko, K. Y.; Woo, W. J.; Kim, Y.; Kim, D.; Lim, J. H.; Lee, S.; Lee, Z.; Park, J.; Kim, H. Low-temperature synthesis of 2D MoS_2 on a plastic substrate for a flexible gas sensor. *Nanoscale* **2018**, *10*, 9338−9345.
(26) Campbell, P. M.; Perini, C. J.; Chiu, J.; Gupta, A.; Ray, H. S.; Chen, H.; Wenzel, K.; Snyder, E.; Wagner, B. K.; Ready, J.; Vogel, E. M. Plasma-assisted synthesis of MoS 2. *2D Mater.* **2017**, *5*, 015005.
(27) Ahn, C.; Lee, J.; Kim, H.-U.; Bark, H.; Jeon, M.; Ryu, G. H.; Lee, Z.; Yeom, G. Y.; Kim, K.; Jung, J.; Kim, Y.; Lee, C.; Kim, T. Low-Temperature Synthesis of Large-Scale Molybdenum Disulfide Thin Films Directly on a Plastic Substrate Using Plasma-Enhanced Chemical Vapor Deposition. *Adv. Mater.* **2015**, *27*, 5223−5229.
(28) Jang, Y.; Yeo, S.; Lee, H.-B.-R.; Kim, H.; Kim, S.-H. Wafer-scale, conformal and direct growth of MoS_2thin films by atomic layer deposition. *Appl. Surf. Sci.* **2016**, *365*, 160−165.
(29) Kim, Y.; Kwon, S.; Seo, E.-J.; Nam, J. H.; Jang, H. Y.; Kwon, S.-H.; Kwon, J.-D.; Kim, D.-W.; Cho, B. Facile Fabrication of a Two-Dimensional TMD/Si Heterojunction Photodiode by Atmospheric-Pressure Plasma-Enhanced Chemical Vapor Deposition. *ACS Appl. Mater. Interfaces* **2018**, *10*, 36136−36143.
(30) Hussain, S.; Singh, J.; Vikraman, D.; Singh, A. K.; Iqbal, M. Z.; Khan, M. F.; Kumar, P.; Choi, D. C.; Song, W.; An, K. S.; Eom, J.; Lee, W. G.; Jung, J. Large-area, continuous and high electrical performances of bilayer to few layers MoS_2 fabricated by RF sputtering via post-deposition annealing method. *Sci. Rep.* **2016**, *6*, 30791.
(31) Sharma, A.; Verheijen, M. A.; Wu, L.; Karwal, S.; Vandalon, V.; Knoops, H. C. M.; Sundaram, R. S.; Hofmann, J. P.; Kessels, W. M. M.; Bol, A. A. Low-temperature plasma-enhanced atomic layer deposition of 2-D MoS_2: Large area, thickness control and tuneable morphology. *Nanoscale* **2018**, *10*, 8615−8627.
(32) Bertolazzi, S.; Bonacchi, S.; Nan, G.; Pershin, A.; Beljonne, D.; Samorì, P. Engineering Chemically Active Defects in Monolayer MoS_2 Transistors via Ion-Beam Irradiation and Their Healing via Vapor Deposition of Alkanethiols. *Adv. Mater.* **2017**, *29*, 1606760.
(33) Lu, A.-Y.; Zhu, H.; Xiao, J.; Chuu, C.-P.; Han, Y.; Chiu, M.-H.; Cheng, C.-C.; Yang, C.-W.; Wei, K.-H.; Yang, Y.; Wang, Y.; Sokaras, D.; Nordlund, D.; Yang, P.; Muller, D. A.; Chou, M.-Y.; Zhang, X.; Li, L.-J. Janus monolayers of transition metal dichalcogenides. *Nat. Nanotechnol.* **2017**, *12*, 744−749.
(34) Zhu, J.; Wang, Z.; Yu, H.; Li, N.; Zhang, J.; Meng, J.; Liao, M.; Zhao, J.; Lu, X.; Du, L.; Yang, R.; Shi, D.; Jiang, Y.; Zhang, G. Argon Plasma Induced Phase Transition in Monolayer MoS_2. *J. Am. Chem. Soc.* **2017**, *139*, 10216−10219.
(35) Liu, Y.; Nan, H.; Wu, X.; Pan, W.; Wang, W.; Bai, J.; Zhao, W.; Sun, L.; Wang, X.; Ni, Z. Layer-by-layer thinning of MoS_2 by plasma. *ACS Nano* **2013**, *7*, 4202−4209.
(36) Xiao, S.; Xiao, P.; Zhang, X.; Yan, D.; Gu, X.; Qin, F.; Ni, Z.; Han, Z. J.; Ostrikov, K. K. Atomic-layer soft plasma etching of MoS_2. *Sci. Rep.* **2016**, *6*, 19945.
(37) Lin, T.; Kang, B.; Jeon, M.; Huffman, C.; Jeon, J.; Lee, S.; Han, W.; Lee, J.; Lee, S.; Yeom, G.; Kim, K. Controlled Layer-by-Layer Etching of MoS_2. *ACS Appl. Mater. Interfaces* **2015**, *7*, 15892−15897.
(38) Jeon, M. H.; Ahn, C.; Kim, H.; Kim, K. N.; LiN, T. Z.; Qin, H.; Kim, Y.; Lee, S.; Kim, T.; Yeom, G. Y. Controlled MoS_2 layer etching using CF_4 plasma. *Nanotechnology* **2015**, *26*, 355706.
(39) Chen, X.; Park, Y. J.; Das, T.; Jang, H.; Lee, J.-B.; Ahn, J.-H. Lithography-free plasma-induced patterned growth of $MoS_2$and its heterojunction with graphene. *Nanoscale* **2016**, *8*, 15181−15188.
(40) Li, H.; Zhang, Q.; Yap, C. C. R.; Tay, B. K.; Edwin, T. H. T.; Olivier, A.; Baillargeat, D. From bulk to monolayer MoS_2: Evolution of Raman scattering. *Adv. Funct. Mater.* **2012**, *22*, 1385−1390.
(41) Lee, C.; Yan, H.; Brus, L. E.; Heinz, T. F.; Hone, J.; Ryu, S. Anomalous Lattice Vibrations of Single- and few layer MoS_2. *ACS Nano* **2010**, *4*, 2695−2700.
(42) Porto, S. P. S.; Krishnan, R. S. Raman effect of corundum. *J. Chem. Phys.* **1967**, *47*, 1009−1012.
(43) Splendiani, A.; Sun, L.; Zhang, Y.; Li, T.; Kim, J.; Chim, C.-Y.; Galli, G.; Wang, F. Emerging photoluminescence in monolayer MoS_2. *Nano Lett.* **2010**, *10*, 1271−1275.
(44) Dhakal, K. P.; Duong, D. L.; Lee, J.; Nam, H.; Kim, M.; Kan, M.; Lee, Y. H.; Kim, J. Confocal absorption spectral imaging of MoS_2: Optical transitions depending on the atomic thickness of intrinsic and chemically doped MoS_2. *Nanoscale* **2014**, *6*, 13028−13035.
(45) Wu, R. J.; Udyavara, S.; Ma, R.; Wang, Y.; Chhowalla, M.; Birol, T.; Koester, S. J.; Neurock, M.; Mkhoyan, K. A. Visualizing the metal-MoS_2 contacts in two-dimensional field-effect transistors with atomic resolution. *Phys. Rev. Mater.* **2019**, *3*, 111001.

https://dx.doi.org/10.1021/acsomega.0c02947
ACS Omega 2020, 5, 21853−21861

(46) Ganta, D.; Sinha, S.; Haasch, R. T. 2-D Material Molybdenum Disulfide Analyzed by XPS. *Surf. Sci. Spectra* **2014**, *21*, 19−27.
(47) Scanlon, D. O.; Watson, G. W.; Payne, D. J.; Atkinson, G. R.; Egdell, R. G.; Law, D. S. L. Theoretical and experimental study of the electronic structures of MoO_3 and MoO_2. *J. Phys. Chem. C* **2010**, *114*, 4636−4645.
(48) Klapper, H. S.; Zadorozne, N. S.; Rebak, R. B. Localized Corrosion Characteristics of Nickel Alloys: A Review. *Acta Metall. Sin.* **2017**, *30*, 296−305.
(49) Bouchoule, A.; Boufendi, L. Particulate formation and dusty plasma behaviour in argon-silane RF discharge. *Plasma Sources Sci. Technol.* **1993**, *2*, 204−213.
(50) Hwang, H. H.; Kushner, M. J. Regimes of particle trapping in inductively coupled plasma processing reactors. *Appl. Phys. Lett.* **1996**, *68*, 3716−3718.
(51) Schweigert, V. A.; Schweigert, I. V. Coagulation in a low-temperature plasma. *J. Phys. D: Appl. Phys.* **1996**, *29*, 655−659.
(52) Ricci, D.; Braga, P. C. *Atomic Force Microscopy*; Humana Press: New Jersey, 2004; Vol. *242*, pp 25−38.
(53) Susman, S.; Clark Rowland, S.; Volin, K. J. The purification of elemental sulfur. *J. Mater. Res.* **1992**, *7*, 1526−1533.

https://dx.doi.org/10.1021/acsomega.0c02947
ACS Omega 2020, 5, 21853−21861